Advanced Fiber Materials
https://doi.org/10.1007/s42765-025-00519-8

RESEARCH ARTICLE

Fabricating Aramid Fibers with Ultrahigh Tensile and Compressive Strength

Ziyi Zhang[1,2,3] · Yongheng Wang[4] · Hang Zhou[2,3] · Hongbo Dai[2,3,5] · Jiajun Luo[6] · Yizi Chen[7,8,9] · Zhaolong Li[2,3,5] · Mengdie Li[2] · Chun Li[3] · Enlai Gao[4] · Kun Jiao[2,3] · Jin Zhang[2,3]

Received: 15 November 2024 / Accepted: 3 February 2025

Abstract

High tensile and compressive strengths are essential for fiber-reinforced plastic utilized in complex loading conditions. However, it is challenging to produce aramid fibers with both high tensile and compressive strengths. In the present work, graphene oxide modified with *p*-phenylenediamine (GO-PPDA) was introduced to simultaneously increase the tensile strength (up to 6.75 GPa) and compressive strength (up to 676.8 MPa) of the heterocyclic aramid fibers. GO-PPDA covalently links polymer molecular chains via amine groups, inducing a regular alignment that enhances crystallinity and orientation. Multi-scale characterization indicates that the two-dimensional graphene oxide (GO) enhances interfacial interactions among molecular chains, nanofibers, and fibril bundles, resulting in reduced sheath-core structural disparity and increased fiber densification. Atomistic simulations demonstrate that the enhancements in orientation, densification, and interfacial interactions of the building blocks contribute to the simultaneous improvement in both the tensile and compressive strengths of composite fibers. Finally, we demonstrate that the exceptional mechanical properties of these fibers can be effectively transferred to their composite materials, which is crucial for practical applications.

Keywords Heterocyclic aramid fibers · Graphene oxide · Tensile strength · Compressive strength · Composite materials

1 Introduction

The origins of aramid fibers can be traced back to the 1960s, marked by DuPont's pioneering development and industrial-scale production [1–3]. Among the most notable representatives is Kevlar®, a poly-*p*-phenylene terephthalamide (PPTA) fiber known for its commercial recognition [4–6]. The exceptional mechanical properties of aramid fibers are intrinsically attributed to their unique molecular chains and structure [7–9]. In pursuit of enhanced mechanical properties, novel heterocyclic aramid fibers (HAFs) have been developed containing heterocyclic monomers such as 2-(4-aminophenyl)-5-aminobenzimidazole (PABZ) [10, 11].

Ziyi Zhang and Yongheng Wang have contributed equally to the work.

✉ Enlai Gao
enlaigao@whu.edu.cn

✉ Kun Jiao
jiaokun-cnc@pku.edu.cn

✉ Jin Zhang
jinzhang@pku.edu.cn

[1] College of Science, China University of Petroleum-Beijing, Beijing 102249, China

[2] School of Materials Science and Engineering, College of Chemistry and Molecular Engineering, Academy for Advanced Interdisciplinary Studies, Peking University, Beijing 100871, China

[3] Beijing Graphene Institute (BGI), Beijing 100095, China

[4] Department of Engineering Mechanics, School of Civil Engineering, Wuhan University, Wuhan 430072, China

[5] College of Chemistry and Chemical Engineering, Ningxia University, Yinchuan 750021, China

[6] School of Advanced Materials, Shenzhen Graduate School, Peking University, Shenzhen 518055, China

[7] China Bluestar Chengrand Chemical Co., Ltd., Chengdu 610041, China

[8] China Bluestar Chengrand Co., Ltd., Chengdu 610041, China

[9] High-Tech Organic Fibers Key Laboratory of Sichuan Province, Chengdu 610041, China

Published online: 20 March 2025

These aramid fibers exhibit complete solubility in organic solvents, facilitating higher rates of stretching during processing. Consequently, HAFs demonstrate superior mechanical performance [12, 13].

In practical applications such as impact protection, vibration damping, and deep-sea pressure vessels, fibers in composite materials are subjected not only to axial loads but also to multi-directional forces, including compression, bending, and shear. To ensure structural stability and extend service life, high-performance fibers must exhibit both high tensile strength and compressive strength. Additionally, the compressive strength of fibers plays a pivotal role in determining the efficiency of stress transfer between the fibers and the matrix. This efficiency is critical for achieving superior mechanical properties in composite materials [14]. Nevertheless, as with most organic fibers, heterocyclic aramid fibers exhibit a notable discrepancy in compressive properties when compared to inorganic fibers [15]. Due to the wet spinning process, the organic fibers exhibit a distinct sheath-core structure [16]. Within this structure, polymer molecular chains are connected via non-covalent bonds, leading to inadequate cohesion within the fiber [17]. These structural limitations make HAF composites prone to fibrillation and splitting under shear stress [18, 19]. To address this issue, various strategies have been proposed, including optimization of the spinning process [20], incorporation of nanocomposites [21–25], and utilization of chemical crosslinking techniques [26–28]. These methods aim to enhance fiber cohesion. However, the main shortcoming of these methods is the inability to increase both compressive and tensile strength simultaneously. For instance, introducing trace amounts of oxygen during spinning to form covalent bonds between polymer molecular chains enhances the compressive performance of fibers [29]. However, this process disrupts fiber orientation, leading to a reduction of tensile strength. Consequently, it is challenging for HAFs to overcome the inherent limitation of simultaneously increasing compressive and tensile strengths while effectively transferring these properties to composite materials.

The manufacturing process of carbon fibers is widely recognized as involving the pre-oxidization and carbonization of polyacrylonitrile fibers, resulting in a strong planar π-π interactions network [30, 31]. Similarly, M5 (poly-pyridobisimidazole, PIPD) fibers have unique molecular structures (such as large quantities of N–H···O and O–H···N) to form strong intermolecular and intramolecular hydrogen bonds [32, 33]. In particular, the two-dimensional (2D) hydrogen bond network structure endows them with higher compressive strength. GO is a 2D material that provides significant mechanical enhancement in high-performance polymer matrices [34–36]. GO establishes strong interactions with polymers, facilitating polymer crystallization. Additionally, GO serves as a template to promote the orientation of molecular chains [37–39]. HAFs have a complex hierarchy of structural features spanning multiple scales, which include molecular chains, nanofibers, and fibril bundles [40]. Figure 1a illustrates the impact of GO-PPDA on the multiscale structures of composite fibers. By combining the planar structure of carbon fiber with the hydrogen bonding network structure of M5, GO-PPDA was incorporated into HAFs to form a three-dimensional (3D) ordered polymer network structure. The composite fibers were prepared through in situ polymerization followed by wet spinning. GO-PPDA acts as a template to facilitate the orderly alignment of molecular chains, thereby achieving high tensile strength. Furthermore, the 2D structural features of GO-PPDA enable it to bind multiple molecular chains, increasing the cohesion between polymer molecular chains, and enhancing the compressive strength of fibers. The introduction of a 3D strong interaction network increases both the tensile and compressive strength of the fibers. Scanning electron microscope (SEM) images of AF and GO-PPDA/AF show smooth surfaces and similar diameters of ~ 13 μm, suggesting GO-PPDA integration does not affect the fiber preparation (Fig. 1b). The tensile (6.75 GPa) and compressive strength (676.8 MPa) of GO-PPDA/AF is highest among literature reports for the simultaneous enhancement of both properties in organic fibers (Fig. 1d) [41–45]. Finally, the excellent tensile strength (2.24 GPa) and compressive strength (331.4 MPa) of the fiber-reinforced plastic indicate that the mechanical properties of these fibers can be effectively transferred to their composites (Fig. 1c).

2 Experimental Section

2.1 Preparation of Aminated Graphene Oxide

The monomer of heterocyclic aramid, *p*-phenylenediamine (PPDA), was selected as the modifying agent for GO to ensure the purity of the heterocyclic aramid system. Amine-modified GO dispersions were fabricated in a one-step process. GO was dispersed in *N*,*N*-dimethylacetamide (DMAc), and its size was reduced through vigorous sonication in an ice-water bath using an ultrasonic cell-breaking system set to 70% power (1600 W). The resulting ultrasonically treated GO dispersion (0.02 g/mL) was transferred to a round-bottom flask, and PPDA (m_{GO}:m_{PPDA} = 1:2) was added for the amination reaction. The amination process was conducted under a nitrogen atmosphere at 25 °C, 60 °C, and 90 °C for 12 h, with simultaneous stirring and reflux. The samples prepared at these temperatures were designated as GO-PPDA-1, GO-PPDA-2, and GO-PPDA-3.

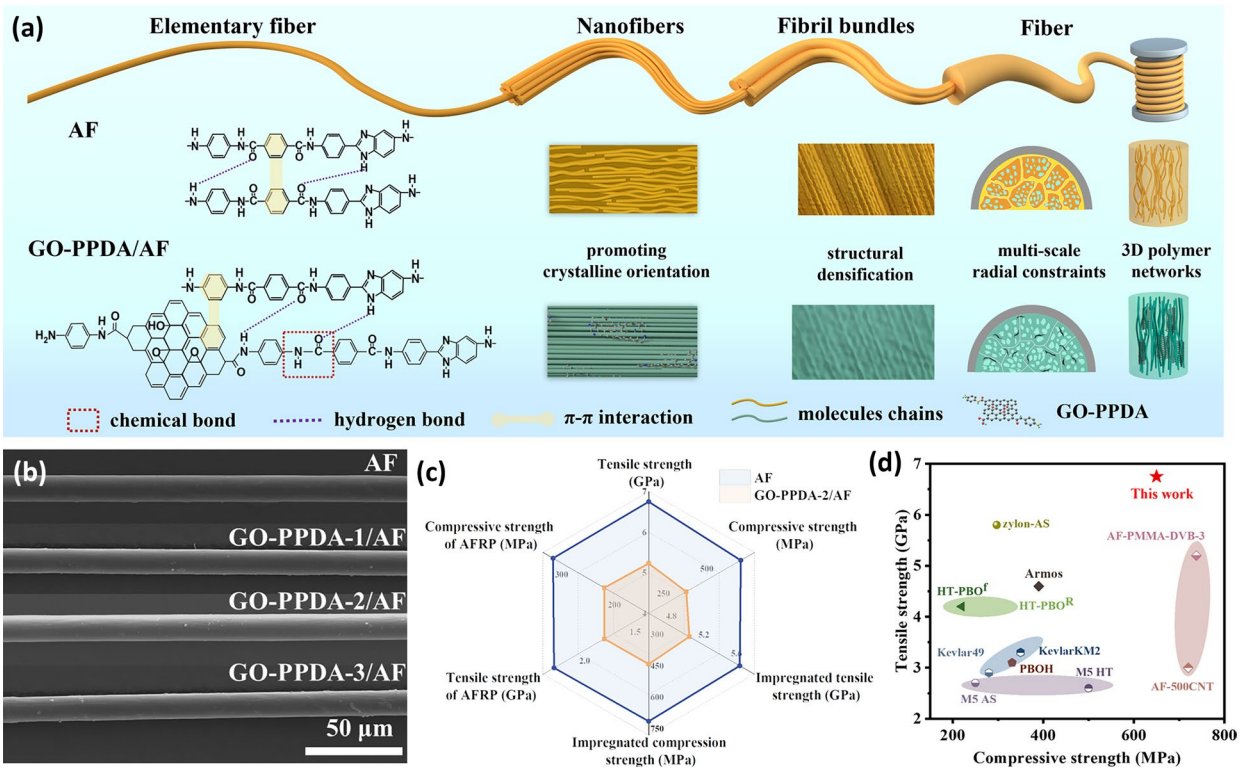

Fig. 1 **a** Schematic diagram of the multi-scale structure of GO-PPDA/AF. **b** SEM images of AF and GO-PPDA/AF. **c** Comparison of mechanical properties of AF and GO-PPDA-2/AF. **d** Comparison of tensile and compressive strength of different organic fibers

2.2 Preparation of AF and GO-PPDA/AF- Spinning Dope

The spinning dope of GO-PPDA/heterocyclic aramid fiber (GO-PPDA/AF) was prepared by in situ polymerization. The polymerization monomers, *p*-phenylenediamine (PPDA) and poly(aminobenzyl) (PABZ), were added to DMAc containing 3.5 wt% lithium chloride (LiCl) and stirred for 40 min until completely dissolved. Subsequently, the GO-PPDA dispersion was added to the solution. After cooling the system to below 10 °C, terephthaloyl chloride (TPC) was added, and the mixture was stirred for 1.5 h. The molar ratio of PPDA, PABZ, and TPC was maintained at 2:3:5. The spinning dope was obtained with a dynamic viscosity of 40,000–60,000 mPa·s. The AF spinning dope was prepared using the same method, excluding the GO-PPDA dispersion. The spinning dopes for GO-PPDA-1/AF, GO-PPDA-2/AF, and GO-PPDA-3/AF were prepared by adding the respective GO-PPDA-1, GO-PPDA-2, and GO-PPDA-3 dispersions.

2.3 Preparation of AF and GO-PPDA/AF via Wet Spinning

The obtained spinning dope was poured into a defoaming kettle and defoamed under a vacuum for 4 h. The spinning dope was then extruded under a nitrogen atmosphere and injected into a two-stage solidification bath, consisting of a primary coagulation bath (50 wt% DMAc and 50 wt% H_2O) and a secondary coagulation bath (20 wt% DMAc and 80 wt% H_2O). The primary fiber was subsequently obtained after washing and drying at 120 °C. Finally, primary fiber was produced following heat treatment at 410 °C in a nitrogen atmosphere. The AF, GO-PPDA-1/AF, GO-PPDA-2/AF, and GO-PPDA-3/AF were prepared under the same procedures by adding corresponding spinning dope.

3 Results and Discussion

3.1 Fabrication and Characterization of GO-PPDA

SEM images show that the average particle size of GO in the dispersion was reduced from approximately 1.25 μm to 0.50 μm to enhance the dispersion performance (Fig. 2a and S1a, b). GO with a sheet size of ~ 500 nm not only enhances the dispersion in DMAc but also this size can span the fiber multilevel structure, enabling the transfer of mechanical loads across scales. The Atomic Force Microscope (AFM) images reveal that the thickness of GO is about 1.0 nm, corresponding to monolayer thickness (Fig. 2b and S1c,

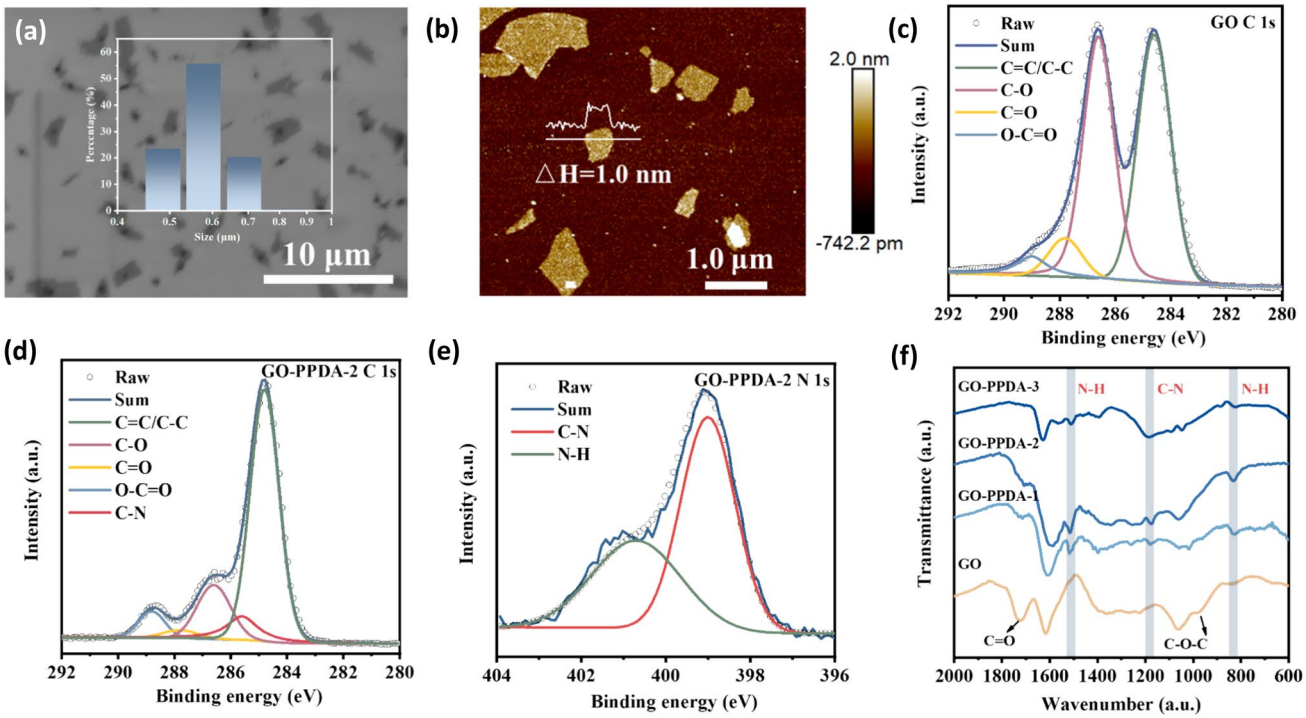

Fig. 2 **a** SEM image of GO. The inset is the lateral size distribution of GO. **b** AFM image of GO. XPS spectra of C 1s of **c** GO and **d** GO-PPDA-2. **e** XPS spectra of N 1s of GO-PPDA-2. **f** FTIR spectra of GO and GO-PPDA

d). Fewer layers of GO can increase the effective interface to enhance stress transfer efficiency [46, 47]. X-ray photoelectron spectroscopy (XPS) peak analysis of C 1s of GO (Fig. 2c) identifies five C signal peaks, C=C/C–C (≈ 284.8 eV), C–O (≈ 286.6 eV), C=O (≈ 287.8 eV) and O—C=O (≈ 288.7 eV) [48–51]. GO with an oxygen content of 44% contains abundant carboxyl functional groups, which serve as reactive centers for the synthesis of GO-PPDA. Additionally, the hydroxyl groups present in GO can form hydrogen bonds with molecular chains, thereby enhancing interfacial interactions between GO and the molecular chains. Figure S2a illustrates the schematic of GO-PPDA. The introduction of amino groups significantly improves the dispersion of GO in DMAc (Fig. S1e, f). XPS spectra of C 1s and N 1 sof GO-PPDA-2 clearly indicate the formation of C-N bonds (Fig. 2d, e), suggesting that the amino group on PPDA reacts with the carboxyl group on GO to form a new C–N covalent bond [52–54]. The number of amine groups in GO increases with increasing temperature (Fig. S2b–f). Fourier-transform infrared (FTIR) spectra show that the peak at 1518 cm^{-1}, attributed to the N–H bending vibration of the amide bond, further confirming the successful introduction of the amine group on GO [55, 56]. Moreover, the carbonyl peak of the GO-PPDA was red-shifted, which was due to the reaction of the carboxyl group with the amine group to form an amide bond and the enhancement of the C=O conjugation effect. The red-shift phenomenon of GO-PPDA-2 is most obvious, which also fully indicates that the amination temperature of 60 °C is the optimal reaction temperature. Excessively high reaction temperatures can result in unfavorable side reactions, including alterations to the surface structure of GO and oxidation of amine groups (Fig. 2f) [57].

3.2 Characterization of GO-PPDA/AF

GO-PPDA served as the fourth monomer in the copolymerization process, leading to the successful preparation of GO-PPDA/AF via wet spinning (Fig. S3a). Transmission electron microscope (TEM) image of the GO-PPDA-2/AF, taken along the radial direction (Fig. 3a), reveals that the sheet size of GO-PPDA-2 within the fiber is approximately 600 nm, consistent with its size in the dispersion solution. Obvious GO lattice stripes were observed by High-resolution transmission electron microscope (HRTEM), confirming the successful preparation of GO-PPDA-2/AF (Fig. 3b). This uniformity indicates that GO-PPDA-2 remains well-dispersed and does not agglomerate during the in-situ polymerization process. The internal structure of the fiber was further demonstrated using AFM (Fig. 3c, d). AF displays a distinct fibril bundle structure, where this relatively loose arrangement is a key factor contributing to the weak radial interactions within the fiber. The fibers are prone to fibrillation when exposed to shear forces. The internal structure of GO-PPDA-2/AF was significantly densified.

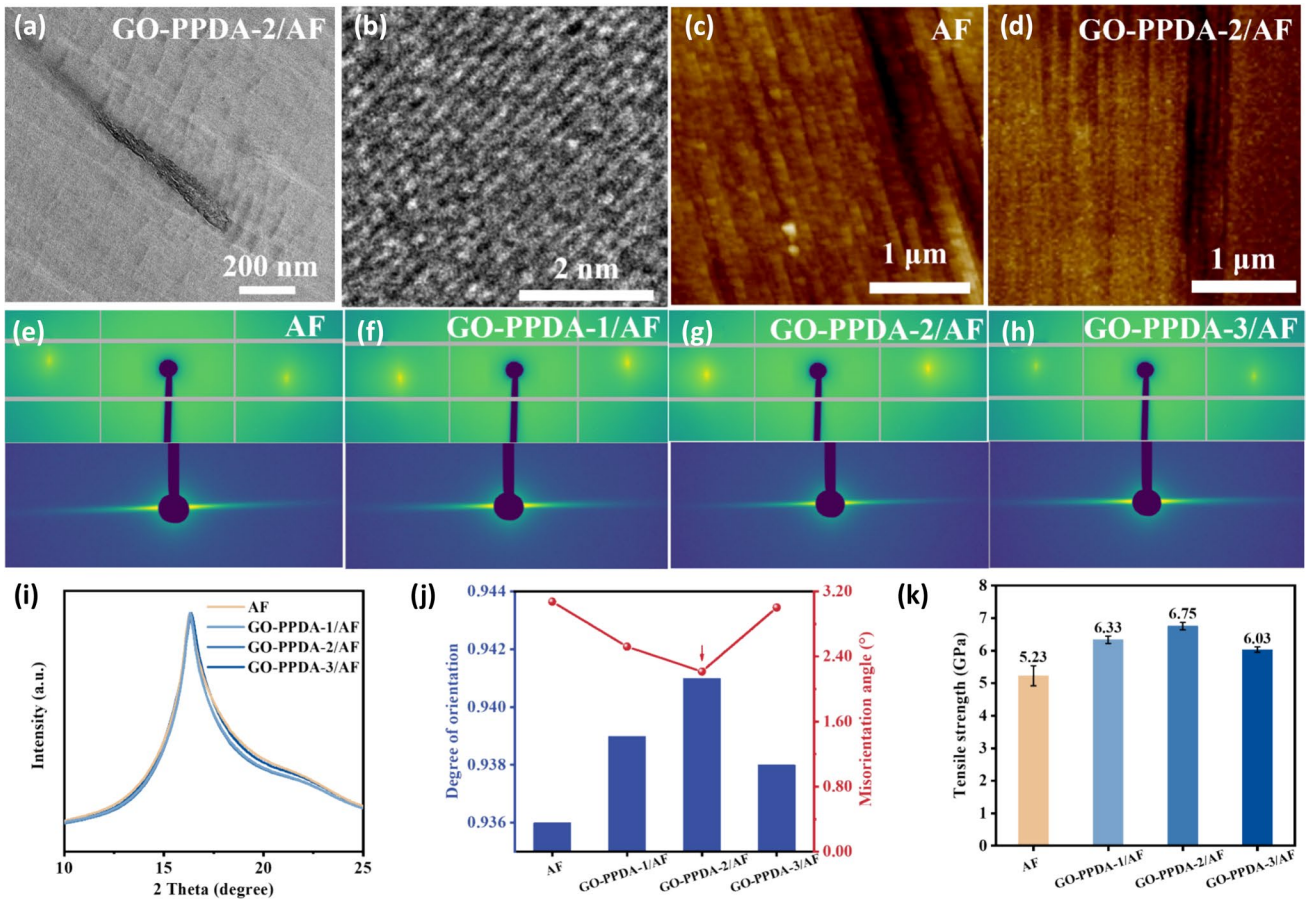

Fig. 3 **a** TEM image and **b** HRTEM image of the axial cross-section of the GO-PPDA-2/AF. AFM morphology of **c** AF and **d** GO-PPDA-2/AF. 2D-WAXS (up) and 2D-SAXS (down) patterns of composite fibers: **e** AF, **f** GO-PPDA-1/AF, **g** GO-PPDA-2/AF, and **h** GO-PPDA-3/AF. **i** 1D-WAXS curves of composite fibers derived from 2D-WAXS analysis. **j** Degree of orientation and comparison of the misorientation angles of different fibers derived from 2D-WAXS and 2D-SAXS analysis. **k** Tensile strength of AF and composite fibers

GO-PPDA can interweave the fibril bundles within the fiber, markedly enhancing radial interactions, and reducing the slip of the molecular chains, thereby improving the mechanical properties of the fiber.

Wide angle X-ray scattering (WAXS) was utilized to evaluate the crystallinity and orientation of the fibers (Fig. 3e–h). The full width at half-maximum (FWHM) of GO-PPDA/AF (GO-PPDA-1/AF: 2.115; GO-PPDA-2/AF: 2.081; GO-PPDA-3/AF: 2.489) was narrower compared to AF (FWHM = 2.547), indicating an improvement in the crystallinity of the composite fiber (Fig. 3i and S3b). By integrating the 2D-WAXS images, azimuthal curves for different fibers were obtained (Fig. 3j). The calculated orientation of the composite fibers (GO-PPDA-1/AF: 0.939, GO-PPDA-2/AF: 0.941, GO-PPDA-3/AF: 0.938) was found to be higher than that of AF (0.936). This indicates that the addition of GO-PPDA improves the orientation of the fibers, but excessive amine functional groups affect the orientation of the fibers. The misorientation angle of microfibers was obtained by small-angle X-ray scattering (SAXS) (Fig. 3e–h). The results demonstrate that the addition of GO-PPDA contributes to decreasing the misorientation angle of microfibers, thereby enhancing their structural alignment (Fig. S3c, 3j). The crystalline regions and microfibers of GO-PPDA-2/AF are optimally oriented.

The addition of GO-PPDA does not impede the polymerization of heterocyclic aramid monomers, confirmed via gel permeation chromatography (GPC) analysis (Fig. S4a, b and Table S1). The SEC-MALS method, which combines size exclusion chromatography (SEC) for separation with multi-angle laser scattering (MALS), was employed to determine the mean square rotation radius (RMS) by analyzing P(θ) at various angles. Plotting log(rms radius) against log(Mw) reveals molecular conformational information. The slope of GO-PPDA-2/AF (0.55) is higher than AF (0.50), which implies that the molecular chains are less entangled (Fig. S4c). The results indicate that GO-PPDA-2 influences the conformation of molecular chains during fiber molding, promoting a more aligned molecular chain orientation, which subsequently enhances tensile strength. The tensile

strength of the composite fiber reached an impressive 6.75 GPa with the addition of 0.05 wt% GO-PPDA-2 (Fig. 3k, S3d–g).

3.3 Radial Structure and Compressive Strength of GO-PPDA/AF

The strength of the intermolecular chain interactions within the fiber was investigated through stress relaxation experiments (Fig. 4a) [58]. The stress relaxation curves indicate that the initial stress retention composite fibers (GO-PPDA-1/AF at 87.0%, GO-PPDA-2/AF at 88.3%, and GO-PPDA-3/AF at 89.0%) are higher than AF (86.0%). The enhanced resistance to interchain slippage in GO-PPDA/AF is attributed to strong interfacial interactions, characterized by covalent bonding and the dense structure formed between GO-PPDA and molecular chains. Moreover, dissolving the fibers in a KOH/DMSO solution enabled the preparation of nanofibers [59]. Compared to AF, GO-PPDA-2/AF exhibited higher resistance to solubilization in the KOH/DMSO solution, indicating stronger interactions between the nanofibers (Fig. S5a–c). To further expose the internal structure of the fibers, they were embedded in resin and sectioned along the axial direction to obtain ultrathin slices (Fig. S5d). The nanoindentation curves (Fig. 4b and S5e–h) revealed that GO-PPDA/AF required a higher load and displayed a higher modulus compared to AF, indicating that the addition of GO-PPDA increased the bonding between the fibril bundles.

The compressive strength of the fibers was evaluated using the tensile recoil test [29]. As shown in Fig. 4c, the addition of GO-PPDA significantly increases the compressive strength of the fibers, with strength progressively increasing in relation to the amine group content. GO-PPDA-3/AF (676.8 MPa) exhibits the highest compressive strength, almost double that of AF (336.6 MPa). The formation of fiber kink bands during recoil is considered a manifestation of compression failure of the fiber. To further analyze the mechanisms underlying the performance improvement, the fiber morphology following the compression tests was examined (Fig. 4d–g). After the compression experiments, fibrillation was evident at the kink bands of the AF. Conversely, the GO-PPDA/AF exhibited significantly reduced damage after the compression testing. Although kink bands were formed, no fibrillation was observed. Moreover, as the number of amine groups increased, the kink band phenomenon was less pronounced, which was attributed to

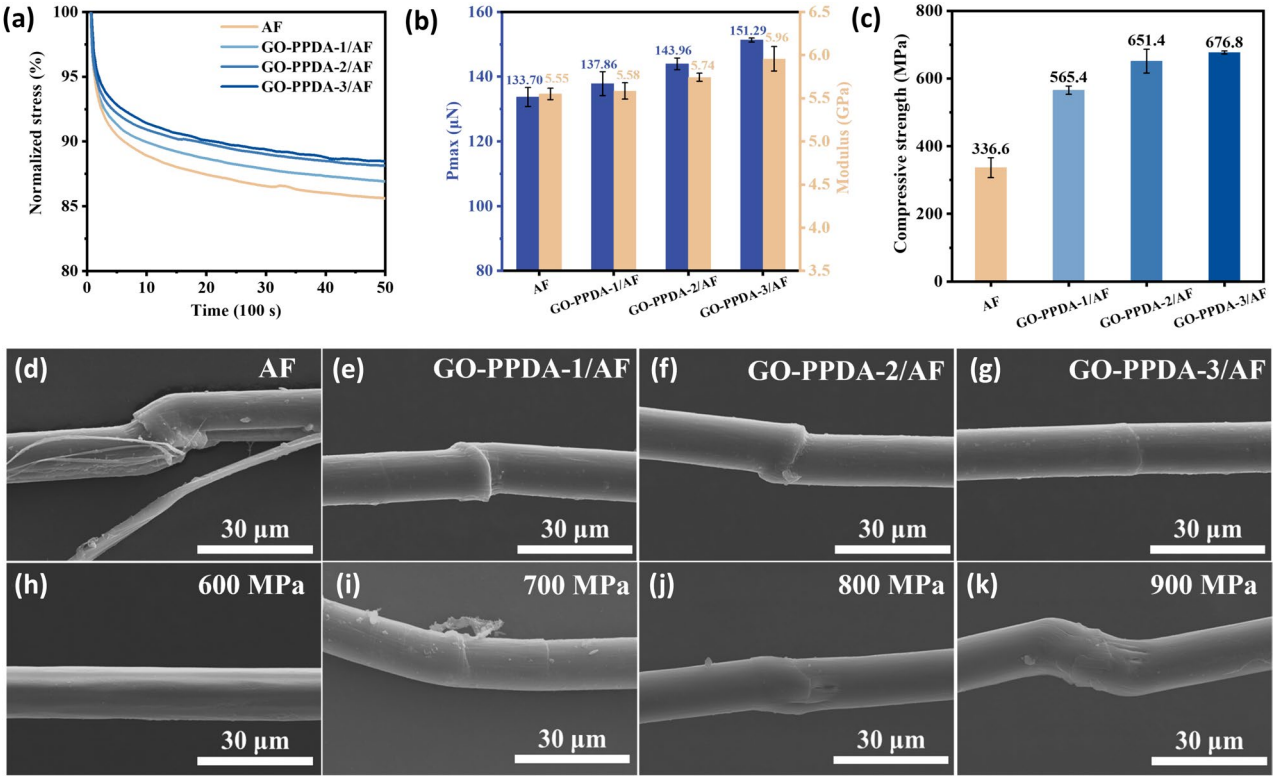

Fig. 4 **a** Stress relaxation curves of different fibers. **b** Peak load results for nanoindentation between fibril bundles indented to a depth of 100 nm. **c** Compression strength of different fibers. The fracture morphology of **d** AF, **e** GO-PPDA-1/AF, **f** GO-PPDA-2/AF, and **g** GO-PPDA-3/AF. The kind bond morphology of GO-PPDA-2/AF after bearing different loads **h** 600 MPa, **i** 700 MPa, **j** 800 MPa, and **k** 900 MPa

enhanced fiber cohesion. GO-PPDA-2/AF was subjected to compression testing at different pressures of 600 MPa, 700 MPa, 800 MPa, and 900 MPa. With increasing pressure, the fiber kinking phenomenon became more pronounced, though fibrillation was not observed (Fig. 4h–k).

3.4 Performance of GO-PPDA/AF Composites

The preparation method for GO-PPDA-2/AF developed in this study is both straightforward and efficient, enabling successful batch production (Fig. S6). The resulting batch-produced GO-PPDA-2/AF yarn exhibits stable performance, achieving a tensile strength of up to 36.53 cN/dtex (Table S2), thus supporting its potential applications in composite materials. To validate the performance of these composites, AF-reinforced plastic (AFRP) and GO-PPDA-2/AF reinforced plastic (GO-PPDA-2/AFRP) were fabricated to further evaluate the tensile and compressive strength of the macro-composites (Fig. 5a–c). Compared to the AFRP, the tensile strength of GO-PPDA-2/AFRP (2.24 GPa) and its compressive strength (331.4 MPa) was enhanced by 28.7% and 41.5%, respectively, indicating effective transfer of mechanical properties from the fibers to the composites (Fig. 5f and S7). The fracture morphology of fiber reinforced plastic was observed by SEM. The fractures of GO-PPDA-2/AFRP consistently exhibited resin residue on the fiber surfaces, whereas AFRP displayed clear resin-fiber separation and significant fiber fibrillation (Fig. 5d, e). This analysis further confirms the improved interfacial interaction and structural integrity achieved through the incorporation of GO-PPDA-2, which consequently enhanced the mechanical properties of the composites.

3.5 Reinforcement Mechanism of GO-PPDA/AF

To understand the microstructural evolution and performance improvement of GO-PPDA/AF, all-atom molecular dynamics simulations and relevant analyses were conducted. First, the atomistic simulations indicate that the introduction of GO-PPDA simultaneously improves the orientation and densification of AF, contributing to enhanced tensile strength (Fig. 6a–c). Meanwhile, the enhanced compressive strength can be attributed to the addition of GO-PPDA, which effectively reduces the slenderness ratios of molecular chains and bundles within GO-PPDA/AF. This reduction improves the critical compressive load required to cause buckling of the molecular chains and bundles, thereby increasing the compressive strength of GO-PPDA/AF (Fig. 6d, e). Furthermore, the stress evolution during the tensile and compressive processes was monitored (Fig. 6f).

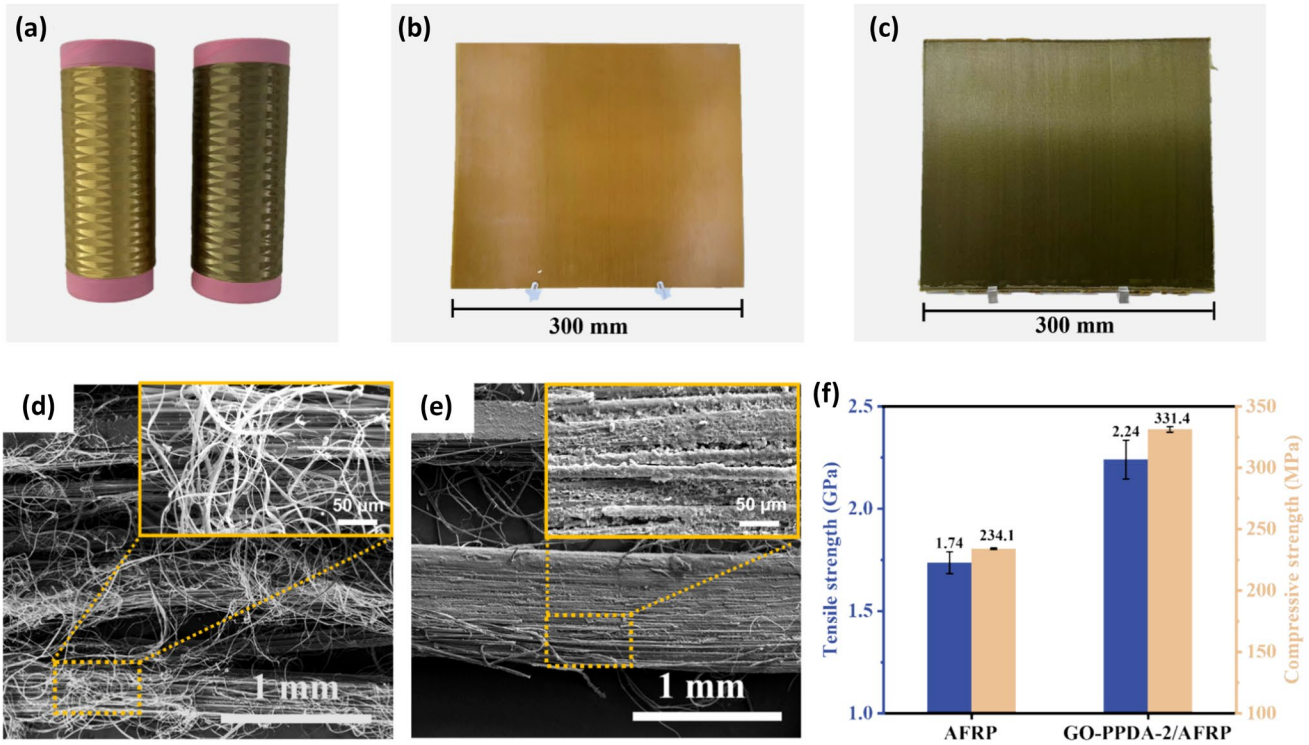

Fig. 5 **a** The digital photograph of AF (left) and GO-PPDA-2/AF (right). Digital photograph of fiber-reinforced plastic made from **b** AF and **c** GO-PPDA-2/AF. **d** AFRP and **e** GO-PPDA-2/AFRP SEM images of fibers after tensile damage. Insets show the corresponding enlarged images of the selected area. **f** Tensile and compressive strength of AFRP and GO-PPDA-2/AFRP

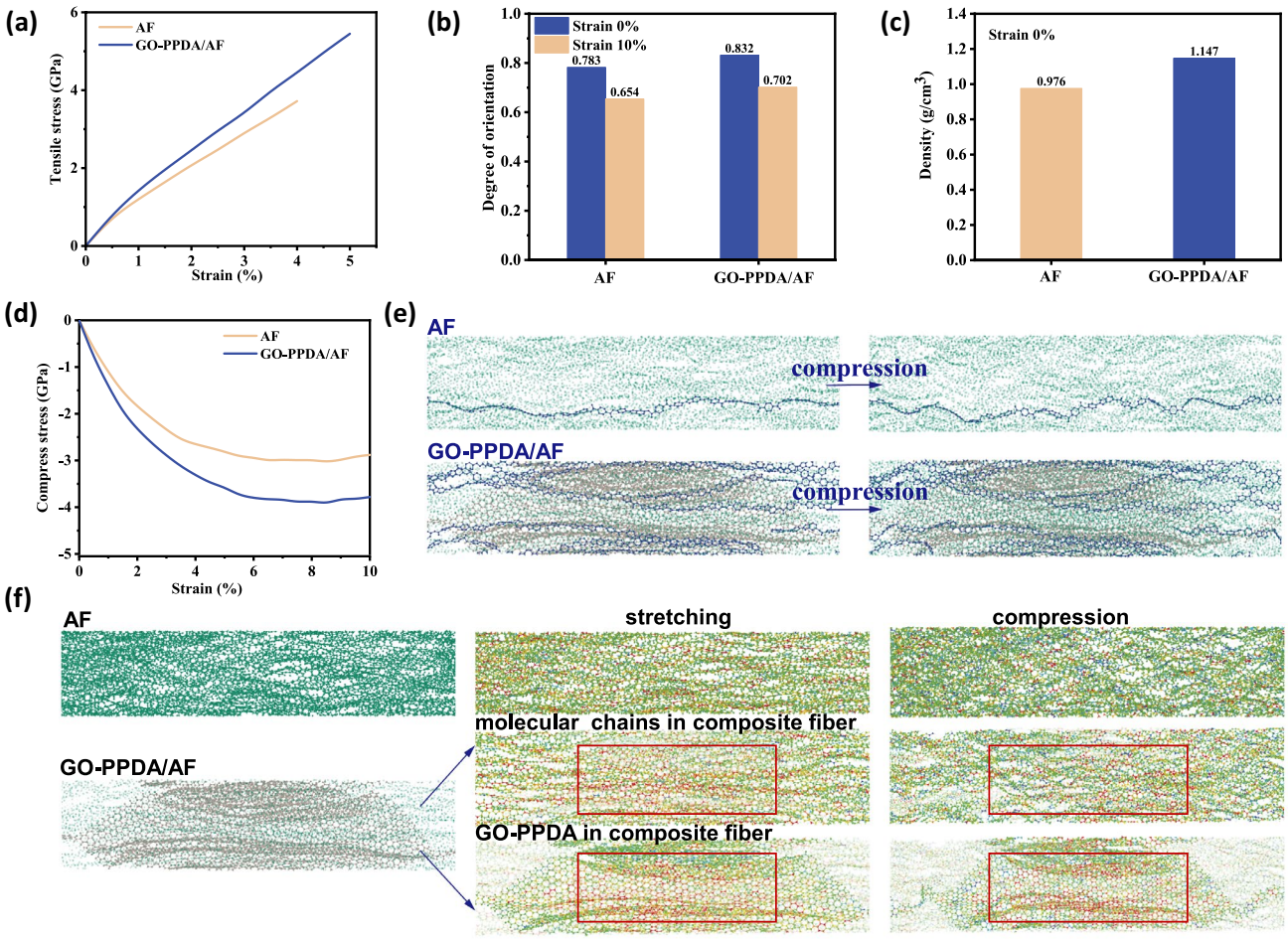

Fig. 6 Atomistic simulations of AF and GO-PPDA/AF. **a** Stress–strain curves of AF and GO-PPDA/AF under tension. **b** Degree of orientation of AF and GO-PPDA/AF under the compressive strains of 0% and 10%. **c** The density of AF and GO-PPDA/AF. **d** Stress–strain curves of AF and GO-PPDA/AF under compression. **e** Morphological evolution of molecular chains within AF and GO-PPDA/AF upon compression. **f** Colormaps of the stress within AF and GO-PPDA/AF under tension and compression. To ensure clarity, we define tensile stress as positive and compressive stress as negative

It was observed that the molecular chains within GO-PPDA/AF are more tightly bound under both tension and compression compared to those within AF. To summarize, the improvements in orientation, densification, and interfacial interactions of the building blocks within GO-PPDA/AF account for the simultaneous enhancement of both the tensile and compressive strengths of these fibers.

4 Conclusions

In summary, this work presents a novel approach to enhance the mechanical properties of HAFs through the incorporation of graphene oxide modified with *p*-phenylenediamine (GO-PPDA). The tensile strength (6.75 GPa) and compressive strength (676.8 MPa) of the obtained fibers were improved simultaneously, which greatly exceeded the values reported in the previous literature. These improvements are attributed to the introduction of GO-PPDA, which aligns polymer molecular chains, enhances crystallinity and orientation, and improves multi-scale interfacial interactions between molecular chains and fibril bundles. These advancements not only improve the mechanical properties of the fibers but also enable effective transfer of these properties into composite materials. This work represents a significant advance in the pursuit of high-performance fiber materials with ultra-high tensile and compressive strength, and has practical guiding implications for engineering scale-up.

Supplementary Information The online version contains supplementary material available at https://doi.org/10.1007/s42765-025-00519-8.

Acknowledgements The authors thank BL10U1 and BL19U2 beamlines of the National Center for Protein Science at the Shanghai Synchrotron for WAXS and SAXS characterization. This work was

financially supported by the Ministry of Science and Technology of China (2018YFA0703502, 2022YFA1203304, and 2022YFA1203302), the National Natural Science Foundation of China (Grant Nos. T2188101, 21972005, 5240130143 and 52021006), the Strategic Priority Research Program of CAS (XDB36030100), and the Beijing National Laboratory for Molecular Sciences (BNLMS-CXTD-202001) and the Shenzhen Science and Technology Innovation Commission (KQTD20221101115627004).

Data availability The data that support the fndings of this study are available from the corresponding author upon reasonable request.

Declarations

Conflict of interest Jin Zhang is an editorial board member-in-chief of Advanced Fiber Materials and was not involved in the editorial review or decision to publish this article. All authors declare that they have no competing interests.

References

1. Chen F, Zhai L, Yang H, Zhao S, Wang Z, Gao C, Zhou J, Liu X, Yu Z, Qin Y, Xu W. Unparalleled armour for aramid fiber with excellent UV resistance in extreme environment. *Adv Sci*. **2021**;*8*:2004171.
2. Minoshima K, Maekawa Y, Komai K. The influence of vacuum on fracture and fatigue behavior in a single aramid fiber. *Int J Fatigue*. **2000**;*22*:757.
3. He A, Xing T, Liang Z, Luo Y, Zhang Y, Wang M, Huang Z, Bai J, Wu L, Shi Z, Zuo H, Zhang W, Chen F, Xu W. Advanced aramid fibrous materials: fundamentals, advances, and beyond. *Adv Fiber Mater*. **2024**;*6*:3.
4. Zhang H, Zhang M, Li J, Yang B, Abbas SC, Fu C, Chen T, Xia Y, Liu J, Du X, He Z, Ni Y. Aramid nanofiber-based functional composite materials: preparations, applications and perspectives. *Compos Part B Eng*. **2024**;*271*:111151.
5. Xu F, Fan W, Zhang Y, Gao Y, Jia Z, Qiu Y, Hui D. Modification of tensile, wear and interfacial properties of Kevlar fibers under cryogenic treatment. *Compos Part B Eng*. **2017**;*116*:398.
6. Dai Y, Meng C, Cheng Z, Luo L, Liu X. Nondestructive modification of aramid fiber based on selective reaction of external cross-linker to improve interfacial shear strength and compressive strength. *Compos Part A Appl Sci Manuf*. **2019**;*119*:217.
7. Rao Y, Waddon AJ, Farris RJ. The evolution of structure and properties in poly(p-phenylene terephthalamide) fibers. *Polymer*. **2001**;*42*:5925.
8. Ding X, Kong H, Qiao M, Hu Z, Yu M. Study on crystallization behaviors and properties of F-III fibers during hot drawing in supercritical carbon dioxide. *Polymers*. **2019**;*11*:856.
9. Şahin K, Clawson JK, Singletary J, Horner S, Zheng J, Pelegri A, Chasiotis I. Limiting role of crystalline domain orientation on the modulus and strength of aramid fibers. *Polymer*. **2018**;*140*:96.
10. Luo L, Wang Y, Dai Y, Yuan Y, Meng C, Cheng Z, Wang X, Liu X. The introduction of asymmetric heterocyclic units into poly(p-phenylene terephthalamide) and its effect on microstructure, interactions and properties. *J Mater Sci*. **2018**;*53*:13291.
11. Xu R, Qiu Y, Tang S, Yang C, Dai Y, Zhang D, Gao Y, Gao K, Luo L, Liu X. Preparation of high strength and toughness aramid fiber by introducing flexible asymmetric monomer to construct misplaced-nunchaku structure. *Macromol Mater Eng*. **2021**;*306*:2000814.
12. Penn L, Milanovich F. Raman spectroscopy of Kevlar 49 fibre. *Polymer*. **1979**;*20*:31.
13. Dobb MG, Johnson DJ, Saville BP. Compressional behaviour of Kevlar fibres. *Polymer*. **1981**;*22*:960.
14. McDaniel PB, Sockalingam S, Deitzel JM, Gillespie JW, Keefe M, Bogetti TA, Casem DT, Weerasooriya T. The effect of fiber meso/nanostructure on the transverse compression response of ballistic fibers. *Compos Part A Appl Sci Manuf*. **2017**;*94*:133.
15. Tanaka F, Okabe T, Okuda H, Kinloch IA, Young RJ. The effect of nanostructure upon the compressive strength of carbon fibres. *J Mater Sci*. **2012**;*48*:2104.
16. Dobb MG, Robson RM. Structural characteristics of aramid fibre variants. *J Mater Sci*. **1990**;*25*:459.
17. Cheng Z, Li X, Lv J, Liu Y, Liu X. Constructing a new tear-resistant skin for aramid fiber to enhance composites interfacial performance based on the interfacial shear stability. *Appl Surf Sci*. **2021**;*544*:148935.
18. Luo L, Yuan Y, Dai Y, Cheng Z, Wang X, Liu X. The novel high performance aramid fibers containing benzimidazole moieties and chloride substitutions. *Mater Des*. **2018**;*158*:127.
19. Stockdale TA, Cole DP, Staniszewski JM, Roenbeck MR, Papkov D, Lustig SR, Dzenis YA, Strawhecker KE. Hierarchical mechanisms of lateral interactions in high-performance fibers. *ACS Appl Mater Interfaces*. **2020**;*12*:22256.
20. Li K, Luo L, Huang J, Wang H, Feng Y, Liu X. Enhancing mechanical properties of aromatic polyamide fibers containing benzimidazole units via temporarily suppressing hydrogen bonding and crystallization. *J Appl Polym Sci*. **2015**;*132*:42482.
21. Zhang Z, Jia X, Li C, Li L, Wen Y, Gao Z, Zhang J, Gao E, Jiao K, Zhang J. Simultaneously enhanced interfacial shear strength and tensile strength of heterocyclic aramid fiber by graphene oxide. *Nano Res*. **2023**;*16*:12286.
22. Yan D, Luo J, Wang S, Han X, Lei X, Jiao K, Wu X, Qian L, Zhang X, Zhao X, Di J, Zhang Z, Gao Z, Zhang J. Carbon nanotube-directed 7 GPa heterocyclic aramid fiber and its application in artificial muscles. *Adv Mater*. **2023**;*36*:2306129.
23. Luo J, Wen Y, Jia X, Lei X, Gao Z, Jian M, Xiao Z, Li L, Zhang J, Li T, Dong H, Wu X, Gao E, Jiao K, Zhang J. Fabricating strong and tough aramid fibers by small addition of carbon nanotubes. *Nat Commun*. **2023**;*14*:3019.
24. Li J, Wen Y, Xiao Z, Wang S, Zhong L, Li T, Jiao K, Li L, Luo J, Gao Z, Li S, Zhang Z, Zhang J. Holey reduced graphene oxide scaffolded heterocyclic aramid fibers with enhanced mechanical performance. *Adv Funct Mater*. **2022**;*32*:2200937.
25. Sharma S, Rawal J, Dhakate SR, Singh BP. Synergistic bridging effects of graphene oxide and carbon nanotube on mechanical properties of aramid fiber reinforced polycarbonate composite tape. *Compos Sci Technol*. **2020**;*199*:108370.
26. Luo J, Wen Y, Li T, Jia X, Lei X, Zhang Z, Xiao Z, Wu X, Gao Z, Gao E, Jiao K, Zhang J. High interfacial shear strength and high tensile strength in heterocyclic aramid fibers with improved interchain interaction. *Adv Funct Mater*. **2023**;*34*:2310008.
27. Dai Y, Feng J, Meng C, Luo L, Qin J, Liu X. Improving interfacial and compressive properties of aramid by synchronously grafting and crosslinking. *Macromol Mater Eng*. **2019**;*304*:1900044.
28. Yuan Y, Dai Y, Meng C, Luo L, Liu X. Improving compressive strength of aramid fiber by introducing carbon nanotube derivates grafted with oligomers of different conformations and controlling its alignment. *Macromol Mater Eng*. **2019**;*304*:1900127.
29. Dai Y, Yuan Y, Luo L, Liu X. A facile strategy for fabricating aramid fiber with simultaneously high compressive strength and high interfacial shear strength through cross-linking promoted by oxygen. *Compos Part A Appl Sci Manuf*. **2018**;*113*:233.
30. Oya N, Johnson DJ. Longitudinal compressive behaviour and microstructure of PAN-based carbon fibres. *Carbon*. **2001**;*39*:635.
31. Markoski LJ, Walker KA, Deeter GA, Spilman GE, Martin DC, Moore JS. Cross-linkable copolymers of poly(p-phenyleneterephthalamide). *Chem Mater*. **1993**;*5*:248.

32. Leal AA, Deitzel JM, McKnight SH, Gillespie JW. Spectroscopic analysis and kinetics of intermolecular hydrogen bond formation in poly-pyridobisimidazole (M5) fiber. *J Polym Sci Part B Polym Phys*. **2009**;*47*:1809.
33. Leal AA, Deitzel JM, McKnight SH, Gillespie JW. Effect of hydrogen bonding and moisture cycling on the compressive performance of poly-pyridobisimidazole (M5) fiber. *Polymer*. **2009**;*50*:2900.
34. Gao Z, Song Q, Xiao Z, Li Z, Li T, Luo J, Wang S, Zhou W, Li L, Yu J, Zhang J. Submicron-sized, high crystalline graphene-reinforced meta-aramid fibers with enhanced tensile strength. *Acta Phys Chim Sin*. **2023**;*39*:2307046.
35. Yu W, Zhang X, Gao X, Liu H, Zhang X. Fabrication of high-strength PET fibers modified with graphene oxide of varying lateral size. *J Mater Sci*. **2020**;*55*:8940.
36. Kinloch IA, Suhr J, Lou J, Young RJ, Ajayan PM. Composites with carbon nanotubes and graphene: an outlook. *Science*. **2018**;*362*:547.
37. Ming X, Wei A, Liu Y, Peng L, Li P, Wang J, Liu S, Fang W, Wang Z, Peng H, Lin J, Huang H, Han Z, Luo S, Cao M, Wang B, Liu Z, Guo F, Xu Z, Gao C. 2D-Topology-seeded graphitization for highly thermally conductive carbon fibers. *Adv Mater*. **2022**;*34*:2201867.
38. Qi Y, Xia Y, Li P, Wang Z, Ming X, Wang B, Shen K, Cai G, Li K, Gao Y, Liu Y, Gao C, Xu Z. Plastic-swelling preparation of functional graphene aerogel fiber textiles. *Adv Fiber Mater*. **2016**;*2023*:5.
39. Wang F, Fang W, Ming X, Liu Y, Xu Z, Gao C. A review on graphene oxide: 2D colloidal molecule, fluid physics, and macroscopic materials. *Appl Phys Rev*. **2023**;*10*:011311.
40. Stockdale TA, Cole DP, Staniszewski JM, Roenbeck MR, Papkov D, Lustig SR, Dzenis YA, Strawhecker KE. Hierarchical mechanisms of lateral interactions in high-performance fibers. *ACS Appl Mater Interf*. **2020**;*12*:22256.
41. Andrews MC, Lu D, Young RJ. Compressive properties of aramid fibres. *Polymer*. **1997**;*38*:2379.
42. Lv J, Yin J, Qin Y, Dai Y, Cheng Z, Luo L, Liu X. Post-construction of weaving structure in aramid fiber towards improvements of its transverse properties. *Compos Sci Technol*. **2021**;*208*:108780.
43. Sweeny W. Improvements in compressive properties of high modulus fibers by crosslinking. *J Polym Sci A Polym Chem*. **1992**;*30*:1111.
44. Cheng Z, Liu Y, Meng C, Dai Y, Luo L, Liu X. Constructing a weaving structure for aramid fiber by carbon nanotube-based network to simultaneously improve composites interfacial properties and compressive properties. *Compos Sci Technol*. **2019**;*182*:107721.
45. Fawaz SA, Palazotto AN, Wang CS. Compressive properties of high performance polymeric fibers. *Compos Sci Technol*. **1993**;*49*:291.
46. Androulidakis C, Sourlantzis D, Koukaras EN, Manikas AC, Galiotis C. Stress-transfer from polymer substrates to monolayer and few-layer graphenes. *Nanoscale Adv*. **2019**;*1*:4972.
47. Gong L, Young RJ, Kinloch IA, Riaz I, Jalil R, Novoselov KS. Optimizing the reinforcement of polymer-based nanocomposites by graphene. *ACS Nano*. **2012**;*6*:2086.
48. Zhang G, Xu Y, Wang L, Wang J, Kuang Y, Sun X. Rational design of graphene oxide and its hollow CoO composite for superior oxygen reduction reaction. *Sci China Mater*. **2015**;*58*:534.
49. Qiu J, Wang D, Geng H, Guo J, Qian S, Liu X. How oxygen-containing groups on graphene influence the antibacterial behaviors. *Adv Mater Interfaces*. **2017**;*4*:1700228.
50. De Silva KKH, Huang HH, Joshi R, Yoshimura M. Restoration of the graphitic structure by defect repair during the thermal reduction of graphene oxide. *Carbon*. **2020**;*166*:74.
51. Li N, Hu Z, Huang Y. Preparation and characterization of nanocomposites of poly(p-phenylene benzobisoxazole) with amino-functionalized graphene. *Polym Compos*. **2018**;*39*:2969.
52. Liu S, Tian J, Wang L, Sun X. A method for the production of reduced graphene oxide using benzylamine as a reducing and stabilizing agent and its subsequent decoration with Ag nanoparticles for enzymeless hydrogen peroxide detection. *Carbon*. **2011**;*49*:3158.
53. Che J, Shen L, Xiao Y. A new approach to fabricate graphenenanosheets in organic medium: combination of reduction and dispersion. *J Mater Chem*. **2010**;*20*:1722.
54. Tian K, Wang J, Cao L, Yang W, Guo W, Liu S, Li W, Wang F, Li X, Xu Z, Wang Z, Wang H, Hou Y. Single-site pyrrolic-nitrogen-doped sp^2-hybridized carbon materials and their pseudocapacitance. *Nat Commun*. **2020**;*11*:3884.
55. Kim NH, Kuila T, Lee JH. Simultaneous reduction, functionalization and stitching of graphene oxide with ethylenediamine for composites application. *J Mater Chem A*. **2013**;*1*:1349.
56. Ershadi M, Javanbakht M, Mozaffari SA, Brandell D, Lee MT, Zahiri B. Facile stitching of graphene oxide nanosheets with ethylenediamine as three dimensional anode material for lithium-ion battery. *J Alloys Compd*. **2020**;*818*:152912.
57. Jin J, Wu XE, Wang Y, Liang H, Zou M, Niu J, Zhang Y. Cross-scale interface engineering for fabricating super-strong and super-tough aramid nanofiber film. *Adv Funct Mater*. **2024**;*2024*:2416511.
58. Yang M, Wang Z, Li P, Liu Y, Lin J, Wang B, Ming X, Gao W, Xu Z, Gao C. Stress relaxation behaviors of graphene fibers. *Carbon*. **2021**;*182*:384.
59. Yang B, Li W, Zhang M, Wang L, Ding X. Recycling of high-value-added aramid nanofibers from waste aramid resources via a feasible and cost-effective approach. *ACS Nano*. **2021**;*15*:7195.

Fabricating aramid fibers with ultrahigh tensile and compressive strength

Ziyi Zhang,[1,2,3#] Yongheng Wang,[4#] Hang Zhou,[2,3] Hongbo Dai,[2,3,5] Jiajun Luo,[6] Yizi Chen,[7,8,9] Zhaolong Li,[2,3,5] Mengdie Li,[2] Chun Li,[3] Enlai Gao,[4*] Kun Jiao,[2,3*] and Jin Zhang[2,3*]

[1.] College of Science, China University of Petroleum, Beijing, 102249, China.

[2.] School of Materials Science and Engineering, College of Chemistry and Molecular Engineering, Academy for Advanced Interdisciplinary Studies, Peking University; Beijing, 100871, China.

[3.] Beijing Graphene Institute (BGI), Beijing, 100095, China.

[4.] Department of Engineering Mechanics, School of Civil Engineering, Wuhan University, Wuhan, 430072, China.

[5.] College of Chemistry and Chemical Engineering, Ningxia University, Yinchuan, 750021, China

[6.] School of Advanced Materials, Shenzhen Graduate School, Peking University, Shenzhen, 518055, China

[7.] China Bluestar Chengrand Chemical Co., Ltd., Chengdu, 610041, China

[8.] China Bluestar Chengrand Co., Ltd., Chengdu, 610041, China

[9.] High-Tech Organic Fibers Key Laboratory of Sichuan Province, Chengdu, 610041, China

---

[#] These authors contributed equally to the work.

[*] Corresponding author. E-mail address: enlaigao@whu.edu.cn (Enlai Gao 1); jiaokun-cnc@pku.edu.cn (Kun Jiao 2); jinzhang@pku.edu.cn (Jin Zhang 3)

Materials

Graphene oxide (GO, XFNANO, ≥98 wt%), dimethylacetamide (DMAc), dimethyl sulfoxide (DMSO) and potassium hydroxide (KOH) were obtained from Macklin. Lithium chloride (LiCl) was obtained from Aladdin. 5-(6)-Amino-2-(4-aminobenzene) benzimidazole (PABZ), p-phenylenediamine (PPDA), and terephthaloyl dichloride (TPC) were obtained from suppliers.

Characterization

Transmission electron microscope (TEM) was recorded using a Talos F200S G2 electron microscope operating at 200 kV. The scanning electron microscope (SEM) images were recorded using a FEI Quattro S, acceleration voltage is 20 kV. The 2D-WAXD patterns were obtained using a Bruker D8 discovery X-ray diffractometer. Small-angle X-ray scattering (SAXS) and wide-angle X-ray scattering (WAXS) experiments were performed on a beamline (BL16B1) at Shanghai Synchrotron Radiation Facility with detectors Pilatus2M and Pilatus900k, respectively. X-ray photoelectron spectroscopy (XPS) spectra were obtained on the Kratos Analytical Axis-Ultra spectrometer. Fourier transform infrared spectra (FTIR) were recorded using Spectrum Nicolet iS50. The Raman spectra were recorded using LabRAM HR Evolution with a 532 nm laser. GO layer numbers and fiber nanoindentation curves were obtained by Atomic Force Microscope (AFM, Bruker Dimension ICON). The size of GO dispersed in DMAc was measured by Particle Size Analyzer (Mastersizer 3000). The mechanical properties of the fibers were determined by the Electromechanical Universal Testing Machine (Shimadzu EZ-LX, 5 N) instrument. Microdroplet embedding-debonding and stress relaxation measurements were obtained by nano-mechanical testing systems (LLQ-T150, Agilent T150). The radial cross-sections of AF and GO-PPDA/AF were cut by Focused Ion beam (FIB, ZEISS Crossbeam 550).

EXPERIMENTAL METHODS

Molecular weight test

The molecular weight of different polymer solutions was investigated by high performance liquid chromatography (1200 HPLC Series, Agilent) with columns in series (PL mixed-d),

MALS detector (DAWN HELEOS II, Wyatt), and dRI detector (Optilab rEX, Wyatt). The mobile phase is dimethylacetamide (DMAc). Before gel permeation chromatography (GPC) testing, the polymer solution was diluted to a concentration of 0.5 mg/ml with DMAc. In order to prevent the chromatographic column from clogging, the solution was filtered with a 0.22 μm filter membrane.

Stress relaxation measurements

Stress relaxation experiments on fibers were obtained with a micro-nano-tensile apparatus (Agilent T150UTM). The test samples were prepared by gluing the fibers onto rectangular paper frames with a specification length of 20 mm using epoxy resin glue, and the samples were loaded between two gripper tables, with the top gripper table applying a uniaxial tensile force to the samples. The initial strain was set at 1.4% and the initial loading was performed at a loading strain rate of 3×10^{-3} s^{-1} and the strain was held for 5000 s to allow for complete relaxation [1].

Nanoindentation Test

To probe the internal morphology of the fibers, the samples were prepared by the Focused Ion Beam (FIB) notching technique. This technique uses FIB to etch from the outer edge of the fiber diameter to the center of the fiber, exposing a rectangular plane inside the fiber. First, the 4 μm × 4 μm inner surface of the fibers was scanned using an atomic force microscope (AFM) to observe the internal structure of the fibers. The samples were then transferred to a nanoindentation bench for testing. Quasi-static nanoindentation (100 nm indentation depth) of internal fiber morphology was performed using a nanoindentation instrument (TI950) and a tapered diamond probe. The loading time during the experiment was 5 s, the holding time was 2 s and the unloading time was 5 s [2].

Quasi-static mechanical property tests of monofilament

The tensile mechanical properties of single fibers were obtained by a nano-tensile tester (Shimadzu EZ-LX, 5 N). Fibers were fixed on rectangular paper frames with 20 mm spacing using epoxy adhesive and left for 24 h. The samples were loaded between two gripper tables, with the top gripper table applying uniaxial tension in the direction perpendicular to the sample. The loading rate was 1 mm·min^{-1}. The diameter of the fibers was measured with an optical microscope before the tensile test [3].

Compressive strength measurement

Compressive strength was tested by tensile recoil test. First, samples for compression testing were prepared by fixing fibers onto rectangular paper frames with a 20 mm marking length using epoxy adhesive. The samples were loaded between two fixture stages, and the top fixture applied a certain stress to the samples along the vertical direction and cut them off quickly when the stress reached a set value. Compression failure was confirmed by observing the formation of kink bands on an optical microscope. The critical value for the formation of kink bands was determined by testing the fiber compressive strength. The calculation of fiber compressive strength follows the formula:

$$\boldsymbol{p = \frac{P_{max}}{\pi r^2}} \quad \textbf{(1)}$$

where the $\boldsymbol{P_{max}}$ is the maximum compression load and $\boldsymbol{r}$ is the fiber radius [4].

Tensile and compression testing of AF reinforced plastic

A single bundle of fibers is wound onto the mold using a CNC-controlled winding machine to set the surface density of the single layer of winding. The adhesive film is then covered during each winding layer and the operation is repeated until the desired surface density of the composite is achieved. Subsequently, molding was carried out on hot press equipment, and the curing process was as follows: increase the temperature to 90 °C, apply pressure 1-2 MPa, and keep it for 60 minutes, then increase the temperature to 110 °C, apply pressure 2-3 MPa, and keep it for 180 minutes. The gum content of AF reinforced plastic (AFRP) and GO-PPDA-2/AF reinforced plastic (GO-PPDA-2/AFRP) is 45% and 43% respectively. After cooling to room

temperature, demold and cut to standard sample size. Fix the aluminum reinforcement pieces to the ends of the sample strip using epoxy resin. Tensile specimen reinforcements are spaced 150 mm apart and 1 mm thick, compression specimen reinforcements are spaced 14 mm apart and 2 mm thick, and the specimen is clamped centrally in the tester's collet so that the centerline of the specimen is aligned with the centerline of the tester's collet. The specimen was loaded continuously at 2 mm·min^{-1} and the load-displacement curve was recorded continuously.

Atomistic calculation

All-atom molecular dynamics simulations were performed using large-scale atomic/molecular massively parallel simulator (LAMMPS) computational package [5], in which the polymer consistent force field (PCFF) was adopted [6]. Periodic boundary conditions were implemented. The long-range electrostatic interactions were described using the Particle-Particle-Particle-Mesh (PPPM) method [7], and the van der Waals interactions were described by the 6/9 Lennard-Jones potential $\varepsilon[2(\sigma/r)^9-3(\sigma/r)^6]$ with a cutoff distance of 1.0 nm.

To investigate the mechanical behaviors of AF and GO-PPDA/AF, tensile and compressive tests were performed. The initial equilibrated conformations were created in an isothermal−isobaric (NPT) ensemble, where the pressure and temperature were controlled as 1 atm and 300 K, respectively. The Newton's equations of motion were integrated with the velocity-Verlet integrator with the time step of 0.5 fs. Upon structural equilibration, the mechanical responses of these structures to tensile and compressive loads were investigated and analyzed. To ensure clarity, we define tensile stress as positive and compressive stress as negative.

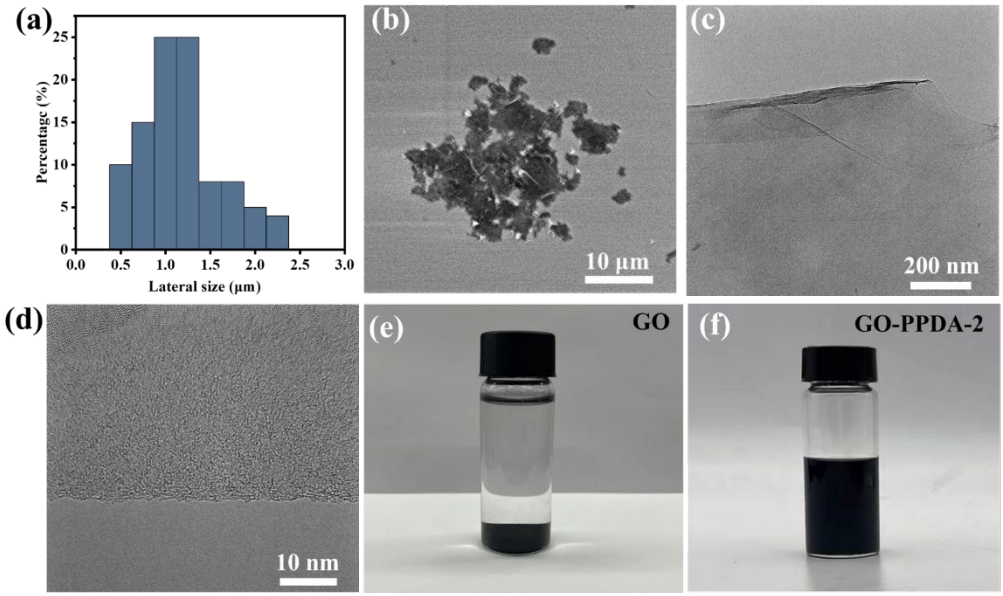

Fig. S1. (a) Lateral size distributions of GO. (b) SEM image of GO. (c) and (d) TEM image of GO. (e) and (f) Digital images of GO and GO-PPDA-2 dispersed in DMAc.

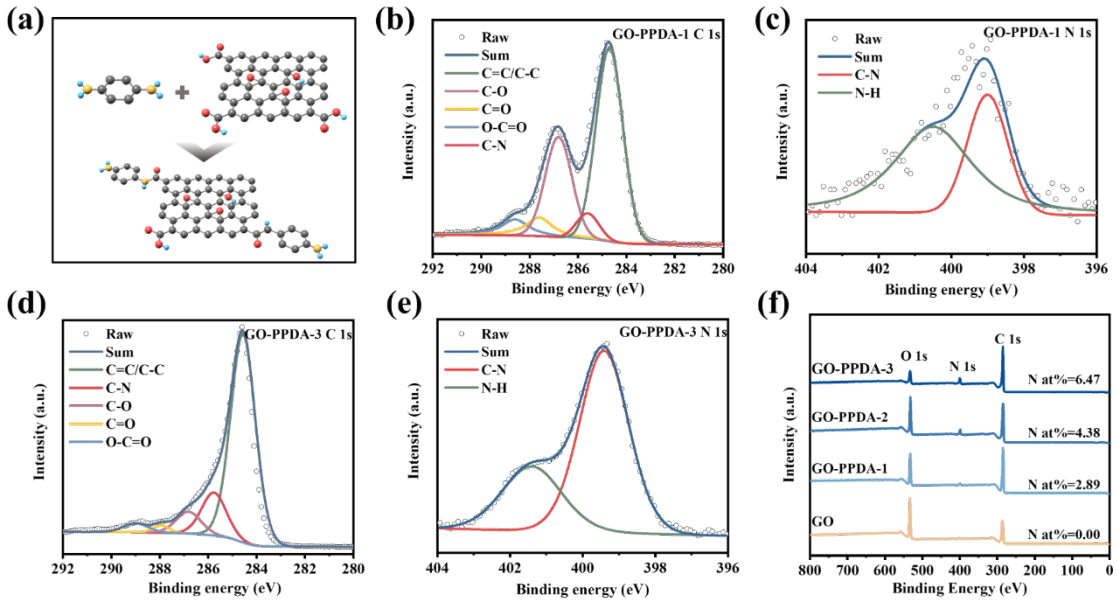

Fig. S2. (a) Preparation procedure of GO-PPDA. XPS spectra of (b) C 1s of GO-PPDA-1, (c) N 1s of GO-PPDA-1, (d) C 1s of GO-PPDA-3, and (e) N 1s of GO-PPDA-3. (f) XPS survey spectra of GO and GO-PPDA.

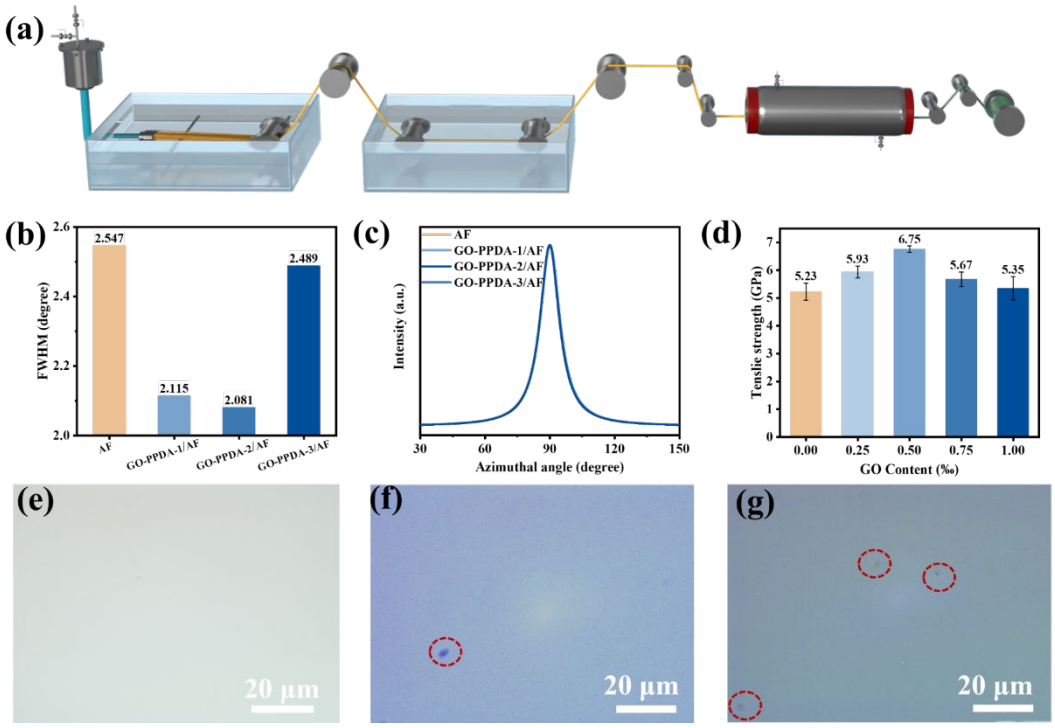

Fig S3. (a) Illustration of the fabrication process of GO-PPDA/AF fibers. (b) Comparison of the FWHM of composite fiber from the 1D-WAXS curves. (c) The azimuthal intensity profile of composite fiber from the 2D-WAXS analysis. (d) Tensile strength of the composite fiber with different GO concentrations. OM images of the copolymerized solution with different addition contents of GO (e) 0.05 wt%, (f) 0.075 wt%, and (g) 0.1 wt%.

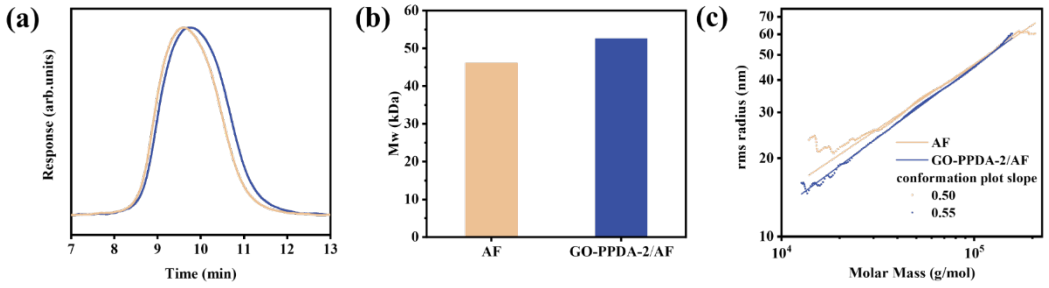

Fig S4. (a) GPC tests of AF and GO-PPDA/AF polymer solutions. (b) The weight-average molecular weight comparison of different polymer solutions. (c) Molecular conformation diagrams of AF and GO-PPDA/AF polymeric solutions.

Table S1 Molecular weight of different polymer solutions determined by GPC method.

Polymer solutions	Mn (kDa)	Mp (kDa)	Mw (kDa)	Mz (kDa)	Polydispersity Mw/Mn
AF	37.69 (±1.65%)	42.31 (±1.54%)	46.10 (±1.57%)	59.14 (±3.53%)	1.22 (±2.28%)
GO-PPDA-2/AF	34.98 (±0.98%)	48.25 (±0.17%)	52.58 (±0.26%)	70.81 (±0.59%)	1.50 (±1.01%)

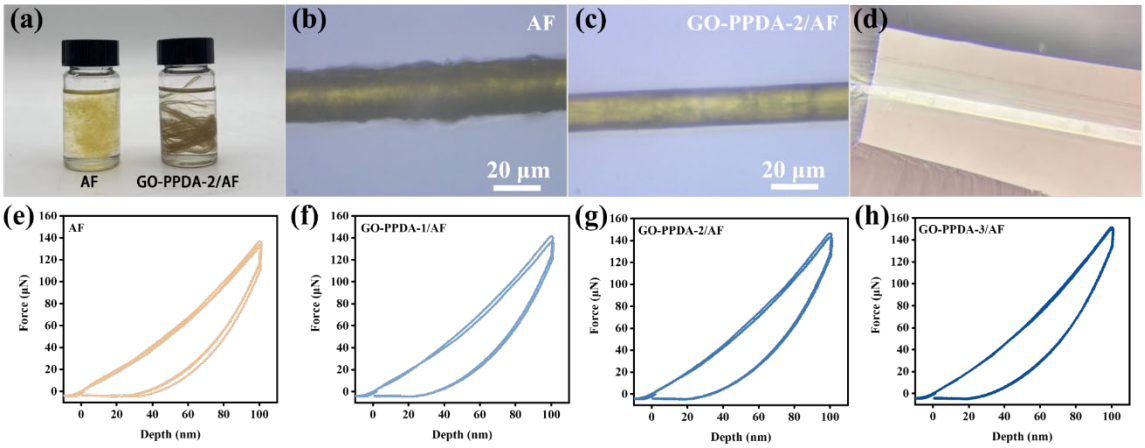

Fig S5. (a) Physical diagram of composite fiber dissolved in KOH/DMSO. OM images of different composite fibers after swelling in KOH/DMSO (b) AF and (c) GO-PPDA-2/AF. (d) OM images of axially sliced cross-sections of composite fibers. Nanoindentation curve of (e) AF and (f) GO-PPDA-1/AF. (g) GO-PPDA-2/AF. (h) GO-PPDA-3/AF.

Fig S6. GO-PPDA-2/AF batch preparation of digital photographs.

Table S2 Tensile strength of GO-PPDA-2/AF yarns prepared in batches.

Number	Tensile strength (cN/dtex)	Modulus (cN/dtex)	Elongation at break (%)
1	**36.53**	**896.09**	**4.20**
2	**36.48**	**887.06**	**4.15**
3	**36.57**	**879.19**	**4.24**
4	**36.60**	**890.98**	**4.24**
5	**36.48**	**883.89**	**4.17**
Average	**36.53**	**887.44**	**4.20**

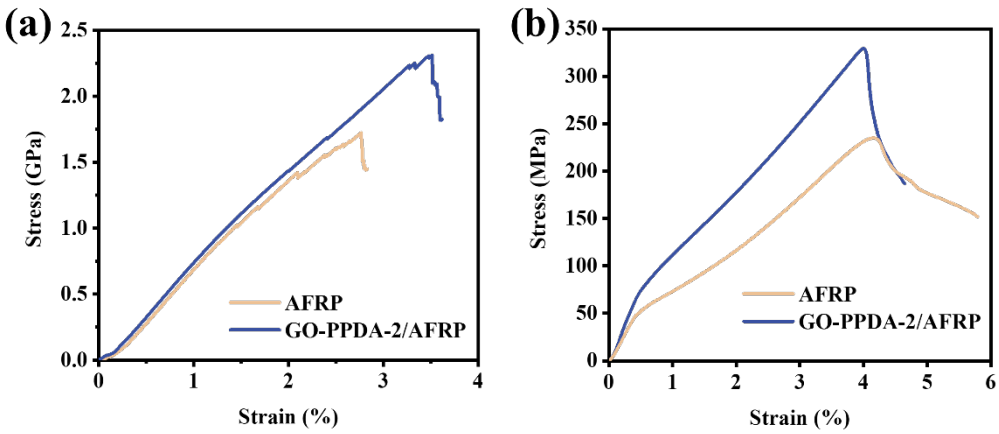

Fig S7. (a) Tensile stress-strain curves of different fiber reinforced plastic. (b) Compressive stress-strain curves of different fiber reinforced plastic.

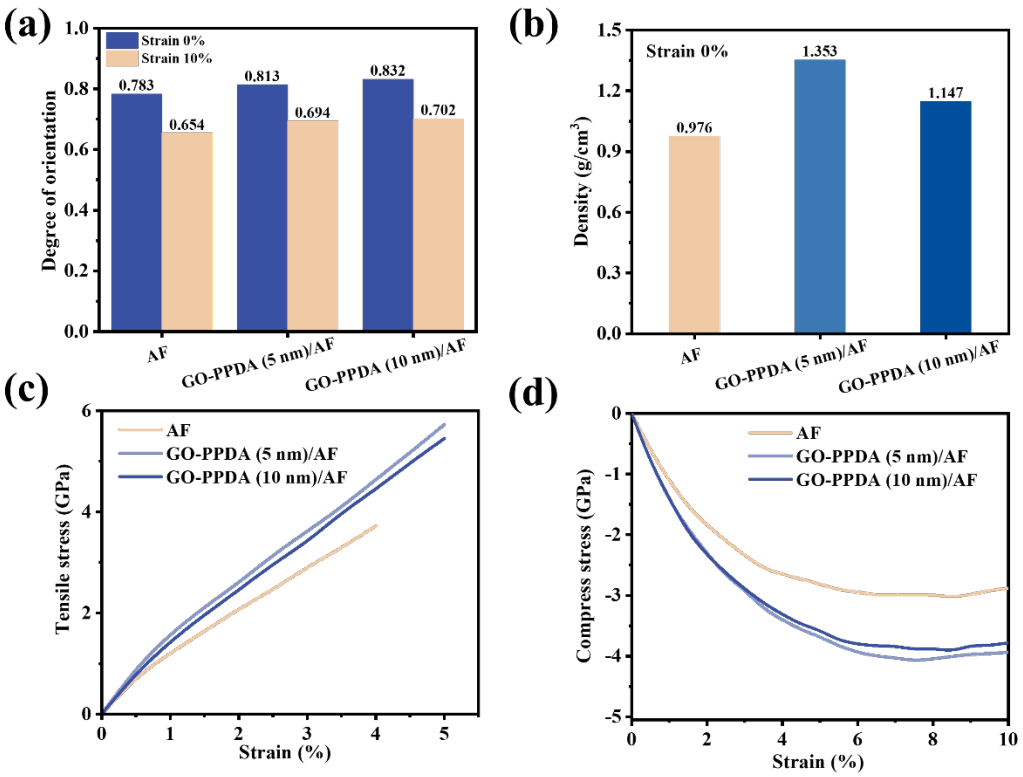

Fig S8. (a) Orientation of AF and GO-PPDA/AF. (b) Density of AF and GO-PPDA/AF. (c) Tensile mechanical properties of AF and GO-PPDA/AF. (d) Compressive mechanical properties of AF and GO-PPDA/AF.

References

[1] Luo J, Wen Y, Li T, Jia X, Lei X, Zhang Z, Xiao Z, Wu X, Gao Z, Gao E, Jiao K, Zhang J. High Interfacial Shear Strength and High Tensile Strength in Heterocyclic Aramid Fibers with Improved Interchain Interaction. *Adv. Funct. Mater.* **2023**, *34*: 2310008.

[2] Yan D, Luo J, Wang S, Han X, Lei X, Jiao K, Wu X, Qian L, Zhang X, Zhao X, Di J, Zhang Z, Gao Z, Zhang J. Carbon Nanotube-Directed 7 GPa Heterocyclic Aramid Fiber and Its Application in Artificial Muscles. *Adv. Mater.* **2023**, *36*: 2306129.

[3] Luo J, Wen Y, Jia X, Lei X, Gao Z, Jian M, Xiao Z, Li L, Zhang J, Li T, Dong H, Wu X, Gao E, Jiao K, Zhang J. Fabricating strong and tough aramid fibers by small addition of carbon nanotubes. *Nat Commun*. **2023**, *14*: 3019.

[4] Yuan Y, Dai Y, Meng C, Luo L, Liu X. Improving Compressive Strength of Aramid Fiber by Introducing Carbon Nanotube Derivates Grafted with Oligomers of Different Conformations and Controlling Its Alignment. *Macromol. Mater. Eng.* **2019**, *304*: 1900127.

[5] Plimpton S. Fast Parallel Algorithms for Short-Range Molecular Dynamics. *J. Comput. Phys.* **1995**, *117*: 1.

[6] Sun H, Mumby SJ, Maple JR, Hagler AT. An ab Initio CFF93 All-Atom Force Field for Polycarbonates. *J. Am. Chem. Soc.* **1994**, *116*: 2978.

[7] Hockney RW, Eastwood JW. Computer simulation using particles. *crc Press*; **1988**. pp. 267-304.